PHYSICAL REVIEW A **86**, 033425 (2012)

Measurements of intense ultrafast laser-driven D_3^+ fragmentation dynamics

A. M. Sayler, J. McKenna, B. Gaire, Nora G. Kling, K. D. Carnes, and I. Ben-Itzhak
J. R. Macdonald Laboratory, Physics Department, Kansas State University, Manhattan, Kansas 66506, USA

(Received 10 August 2012; published 24 September 2012)

Experiments on the triatomic hydrogen molecular ion in intense ultrashort laser pulses are important for understanding the fundamentals of polyatomic molecular dynamics and for providing a benchmark for theory. Here we extend our earlier measurements [Phys. Rev. Lett. **103**, 103004 (2009)] to provide a comprehensive picture of D_3^+ fragmentation in 7- and 40-fs, 790-nm laser pulses at intensities up to 10^{16} W/cm^2. Our measurements incorporate two- and three-body coincidence three-dimensional momentum imaging involving a crossed-beam setup. We provide details of the relative fragmentation rates of all the possible breakup channels as a function of intensity, as well as kinetic energy release and angular distributions.

DOI: 10.1103/PhysRevA.86.033425 PACS number(s): 33.80.Wz, 42.50.Hz

I. INTRODUCTION

One of the most vibrant areas of atomic and molecular physics is the exploration of the dynamics of atoms and molecules exposed to intense ultrashort laser pulses [1–4]. The problems under consideration typically present considerable challenges, both experimentally and theoretically. Advances in experimental techniques, such as coincidence measurements [4–6], allow the investigation of ever more complicated and interesting systems. At the same time, developments in theoretical tools, accompanied by improved computational power, have enabled the modeling of complex atomic and molecular dynamics [7–9]. Certainly, one of the most desirable goals is to develop an enhanced understanding of how polyatomic molecules react to the extreme conditions within a strong laser field [10,11].

Like any problem, it is natural to begin with the simplest system and develop the fundamental knowledge necessary to tackle larger systems. This is why recent experimental studies of D_3^+ in intense femtosecond laser pulses, by ourselves [12] and others [13], present a benchmark for exploring polyatomic molecular dynamics. The H_3^+ and D_3^+ molecules are the most basic stable triatomic molecules, consisting of three nuclei bound by two electrons in a rather unusual equilateral triangle configuration in their ground state (see Fig. 1).

While there have been several theoretical studies of H_3^+ and D_3^+ (or H_3^{2+}) in intense laser pulses (see Refs. [15–26]), the most relevant to our original experimental work [12] is the classical model of the nuclear and electron dynamics presented by Lötstedt *et al.* in recent publications [15,16]. These calculations give a good qualitative description of our experimental results in Ref. [12] and shed additional light on the mechanisms involved in D_3^+ fragmentation.

In this paper we present comprehensive experimental results from investigation of D_3^+ fragmentation in intense ultrashort laser pulses. Using 7- and 40-fs, 790-nm pulses with intensities up to 10^{16} W/cm^2, we explore all possible breakup channels, measured and uniquely identified by coincidence three-dimensional (3D) momentum imaging [5]. Kinetic energy release (KER) and angular distributions for each of the channels are determined from the momenta of the fragments, giving important insight into the strong-field dynamics of D_3^+ fragmentation. Our results are likely to provide stimulus and a benchmark for further theory on this molecule as well as more complex molecules in the future.

II. EXPERIMENTAL METHOD

Details of the experimental setup have been described in our earlier publications on D_3^+ [12,27,28] and other small molecules [5,29]. Thus, we refer the interested reader to the literature and only briefly relay the salient points here.

A beam of vibrationally excited D_3^+ ions, produced in an electron cyclotron resonance (ECR) ion source, is transported at 10-keV beam energy to a laser interaction region. The precise vibrational population distribution of the molecular ions is unknown but is expected to peak at approximately 2 eV (with a full-width half-maximum of ∼1.5 eV) above the minimum of the D_3^+ X^1A' ground-state well [30]; see Ref. [27] for further information. Moreover, by the time the ions reach the interaction point with the laser, their vibrational population is incoherent. In the interaction region, the ion beam is crossed at 90° with a focused laser beam (see Fig. 2) originating from a Ti:sapphire 790-nm laser system. The laser beam consists of linearly polarized 40-fs pulses at 1-kHz repetition rate that can be compressed in duration to 7-fs using a hollow-core fiber and chirped mirrors pulse compression technology (see Ref. [31] for laser system details). The laser polarization is orthogonal to both the ion's and laser beam's propagation directions. The highest peak focal intensity for both pulse durations is 10^{16} W/cm^2 and lower intensities are sampled by crossing the ion beam with the laser away from the center of the laser focus, that is, shifting the laser focus along its propagation direction while keeping the ion beam position fixed (e.g., Refs. [32–34]), a variant of the intensity selective scanning (ISS) method [35,36].

Following laser-induced fragmentation of the D_3^+, the ion beam velocity carries the fragments, except electrons, to a position- and time-sensitive detector operating in event mode. A longitudinal electrostatic spectrometer, situated in the laser–ion beam interaction region, accelerates the charged fragments towards the detector so that ions with different charge-to-energy ratio, and neutral fragments, can be separated by time of flight (TOF). The primary ion beam is collected in a Faraday cup that blocks a small portion at the center of

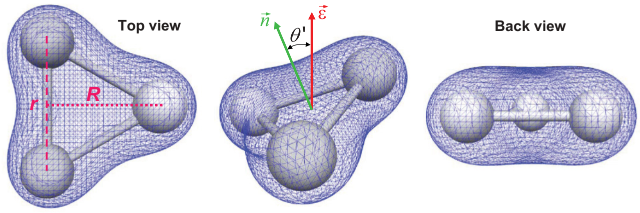

FIG. 1. (Color online) Orbital images of the $D_3{}^+$ ion calculated by C. B. Madsen [14] using GAMESS-US. The positions of the D^+ nuclei are represented by the schematic spheres.

the detector. The fragments (neutral and ionic) are detected in coincidence with the other fragments from the same molecule; hence, each individual fragmentation channel is uniquely identified. In the case of two-body breakup, a double coincidence is required, and for three-body fragmentation, a triple coincidence is required. From the TOF and positions of the fragments, kinematically complete information on the nuclear dynamics is retrieved, leading to KER and angular distributions for $D_3{}^+$ breakup.

III. RESULTS AND DISCUSSION

A. Intensity dependence

We start by surveying the intensity dependence of $D_3{}^+$ fragmentation rates as presented in Fig. 3. The figure shows results from (a) 7-fs and (b) 40-fs pulses spanning the intensity range $\sim 10^{14}$–10^{16} W/cm^2. The fragmentation rate for each channel has been normalized to the ion beam current (∼5 nA) and corrected for the detection efficiency of the detector (measured *in situ* [37]) as well as the changing interaction volume from the ISS method [34].

Evidently there are six fragmentation channels for $D_3{}^+$. These can be categorized as dissociation,

$$\begin{aligned} D_3{}^+ + N\omega &\rightarrow D^+ + D_2 \\ &\rightarrow D_2{}^+ + D \\ &\rightarrow D^+ + D + D, \end{aligned} \tag{1}$$

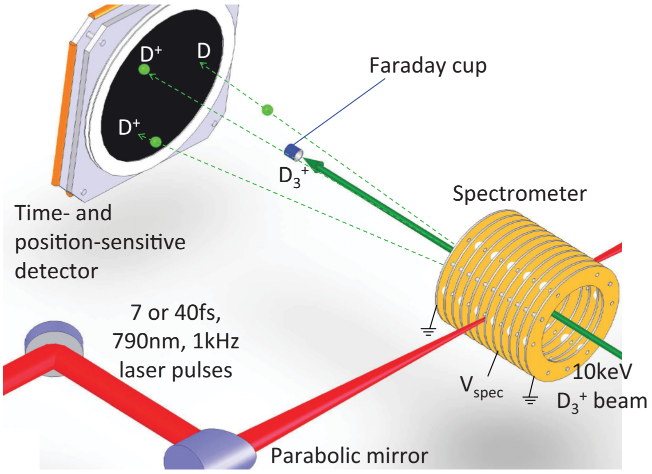

FIG. 2. (Color online) Schematic of the crossed-beam coincidence 3D momentum imaging setup used to measure two-body and three-body laser-induced fragmentation of $D_3{}^+$.

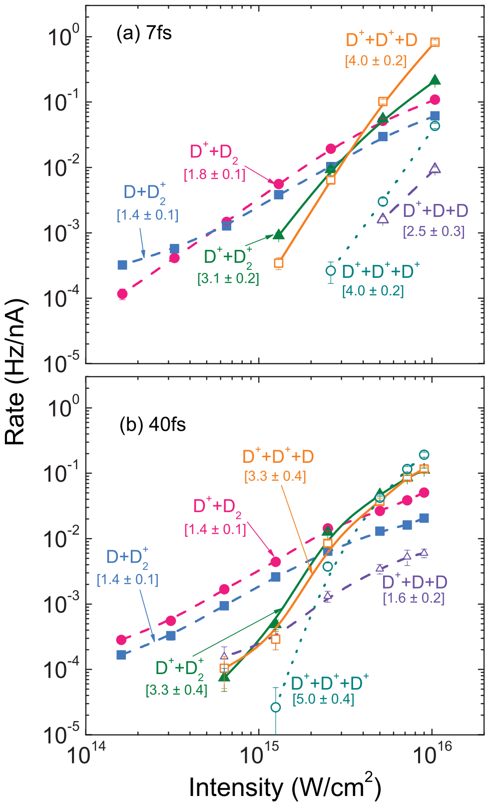

FIG. 3. (Color online) Intensity dependence of the fragmentation rate of $D_3{}^+$ into the dissociation, single-ionization, and double-ionization channels (as labeled) for (a) 7-fs and (b) 40-fs, 790-nm laser pulses at 1-kHz repetition rate. Note that the fragmentation rates are normalized to the ion beam current (in nA), as well as corrected for the detector efficiency and scaled by the relative laser focal volume for the ISS method [34]. The values in parentheses beside each channel label denote approximately the slope m of the trends following an I^m power law, where I is the intensity. The error bars are within the size of the symbols wherever not visible.

single ionization,

$$\begin{aligned} D_3{}^+ + N\omega &\rightarrow D^+ + D_2{}^+ + e^- \\ &\rightarrow D^+ + D^+ + D + e^-, \end{aligned} \tag{2}$$

and double ionization,

$$D_3{}^+ + N\omega \rightarrow D^+ + D^+ + D^+ + 2e^-, \tag{3}$$

where $N\omega$ denotes the multiphoton interaction with the strong laser field (with laser frequency $\omega = 0.058$ a.u. for 790-nm light).

Our results show that dissociation for both pulse durations is dominated by the two-body $D^+ + D_2$ and $D + D_2{}^+$ channels rather than the three-body $D^+ + D + D$ channel. Indeed the actual rates for the two-body channels are expected to be higher than those presented due to losses near 0 eV caused by the Faraday cup (see Ref. [28]). We qualitatively interpret the dominance of two-body breakup from the topology of the $D_3{}^+$ potential energy surfaces (PESs) shown in Figs. 4(a) and 4(b). While these PESs are field free and therefore subject to distortions in the strong laser field, in general the slopes of the potential on both the ground and first-excited state surfaces appear to favor the $D^+ + D_2$ and $D + D_2{}^+$ pathways,

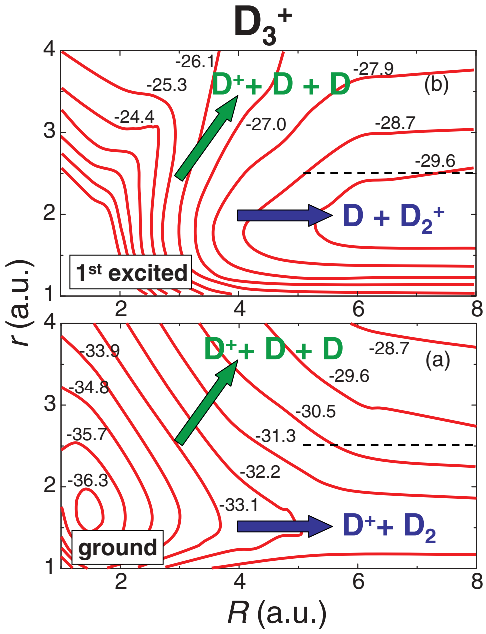

FIG. 4. (Color online) Contour maps of the ground and first-excited state PESs of D_3^+, (a) and (b) respectively, calculated in Ref. [38]. The distances r and R are defined in Fig. 1. Energies of contours are given in electron volts and quoted relative to the $D^+ + D^+ + D^+$ separated-atoms limit. The dashed lines indicate the position where there is an avoided crossing between the ground and first-excited state of D_3^+ [38]. The blue (dark gray) and green (light gray) arrows illustrate the C_S and D_{3h} symmetry stretch directions leading to two- and three-body breakup, respectively.

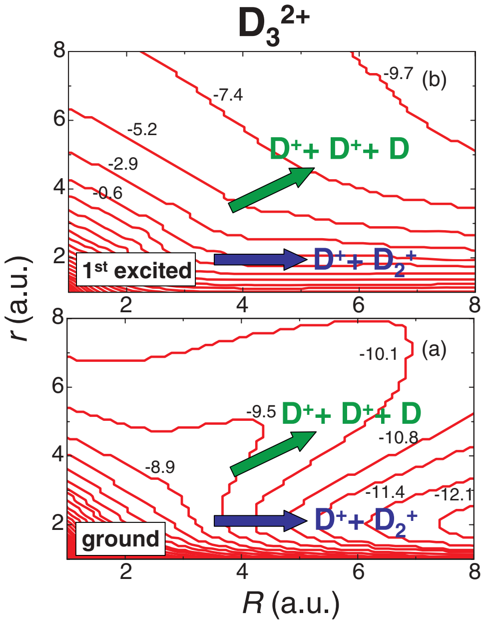

FIG. 5. (Color online) Contour maps of the ground and first-excited state PESs of D_3^{2+}, (a) and (b) respectively, calculated by solving the Born-Oppenheimer equation in three dimensions using B splines [12]. The distances r and R are defined in Fig. 1. Energies of contours are given in electron volts and quoted relative to the $D^+ + D^+ + D^+$ separated-atoms limit. The blue (dark gray) and green (light gray) arrows illustrate the C_S and D_{3h} symmetry stretch directions leading to two- and three-body breakup, respectively.

rather than $D^+ + D + D$. This is evident by the valley in the direction of two-body dissociation, which is likely to funnel a wave packet propagating on the surface towards it (the valley is at fixed $r \sim 1.5$ a.u. for the ground-state surface leading to $D^+ + D_2$, and $r \sim 2.0$ a.u. for the first-excited state surface leading to $D + D_2^+$).

One may attempt to interpret single ionization in a similar way by examining the D_3^{2+} PESs shown in Figs. 5(a) and 5(b). The ground-state D_3^{2+} surface is accessible to both two-body and three-body fragmentation with, arguably, the two-body pathway being favored due to a deeper potential valley. The topology of the first-excited state surface, however, strongly favors three-body fragmentation as it is sloped in that direction. We anticipate that this is why, for 7-fs pulses, the three-body $D^+ + D^+ + D$ channel dominates over the two-body $D^+ + D_2^+$ channel at the highest intensities where excitation to the upper state is more likely. For 40-fs, however, the rates of both channels are comparable, indicating more fragmentation on the lower surface, likely to occur on the rising edge of this longer pulse.

While for most of the channels the fragmentation rates in 7-fs and 40-fs pulses are comparable (within about a factor of 3), double ionization is more than one order of magnitude more probable for 40-fs pulses. This may not appear surprising as typically for longer pulse durations molecules are afforded more time to stretch during the pulse, making it easier to reach higher ionization thresholds as the energy gap between PESs is lower. Additionally, at larger internuclear separations one might anticipate that charge-resonance enhanced ionization plays a role [19] as evident, for example, in the strong-field dynamics of H_2 [39–41]. However, as we show in Sec. III D, stretching of the D_3^+ molecule prior to double ionization is minimal—it starts from an internuclear separation of $r \sim 3.0$ a.u. and stretches to $r \sim 3.2$ a.u. at 7-fs and $r \sim 3.4$ a.u. at 40-fs. Thus it is unclear at this stage what is the reason for the increased probability of double ionization at 40-fs, and we hope that in the future theory may shed some light on this question.

The intensity trend of the rates in Fig. 3 can be approximated by an I^m power-law scaling, where I is the intensity and m the slope. For each fragmentation channel, the approximate slope, m, is denoted in brackets in Fig. 3. Typically, in the perturbative regime m would relate to the number of photons absorbed (lowest-order perturbation theory). However, at the high intensities used in our experiments this relation breaks down and m is anticipated to be smaller [42]. As the figure shows, this is the case since, for example, ionization of D_3^+ to D_3^{2+} requires a minimum of nine photons at 790 nm while m for the single-ionization channels is around 3–4. It also follows that m increases from about 1.4 for dissociation to 5.0 for double ionization, as one expects since double ionization is a higher order nonlinear process than dissociation. The slope of the $D^+ + D + D$ channel is greater than the $D^+ + D_2$ and $D + D_2^+$ channels consistent with the fact that the dissociation pathway for the $D^+ + D + D$ channel is energetically harder to access [13]. Furthermore, at 7-fs, the slope of the $D^+ + D^+ + D$ channel is greater than the $D^+ + D_2^+$, providing additional support for the D_3^{2+} ground state leading to two-body breakup and the excited state leading to three-body breakup.

In general, the agreement of the intensity trends from the classical calculations of Lötstedt *et al.* [15,16] with this experimental data is reasonable. The authors report that the classical calculations were carried out for 3.9-fs pulses, shorter than those used in our experiment, but that they do account for focal-volume intensity averaging present in the experiments and also include a vibrational energy spread aimed to mimic the assumed experimental distribution. There are, however, several noticeable differences between the experimental trends and the calculations of Lötstedt *et al.* For example, the $D^+ + D + D$ channel plays a much larger role in the simulations than we observe in our experiments. In addition, the $D^+ + D_2$ channel was found to be relatively much weaker (factor of $\sim 10^2$) than the $D + {D_2}^+$ channel, which clearly disagrees with our data. Whether these discrepancies are due to differences in experiment and simulation conditions, are an oversimplification of the classical model (such as the model potentials as suggested in Refs. [15,16]), or are due to some other cause remains to be seen.

Finally, we make one last observation concerning fragmentation rates. Under similar conditions, the fragmentation rate of ${D_3}^+$ is considerably lower than other small molecular ions that we have studied [43]. For example, for 7-fs at 5×10^{15} W/cm^2, the dissociation rate for ${D_3}^+ \rightarrow D^+ + D_2$ is a factor of ~ 3.8 lower than ${N_2}^+ \rightarrow N^+ + N$, ~ 6.6 lower than ${O_2}^+ \rightarrow O^+ + O$, and ~ 80 lower than ${H_2}^+ \rightarrow H^+ + H$. This agrees with the fact that below $\sim 10^{14}$ W/cm^2 the dissociation rate of ${D_3}^+$ is extremely low. We believe this is an indication of the high stability of the ${D_3}^+$ triangle in its ground state that requires high intensity to initiate excitation to the repulsive first-excited state. For instance, the main ${D_3}^+$ dissociation pathways that are noted in Sec. III B all require the initial absorption of at least three photons, compared with the dissociation of H_2^+ that requires only the absorption of one photon [5].

B. Dissociation

1. $D^+ + D_2$ channel

As discussed in Sec. III A, the rate of three-body dissociation is low, so here we concentrate mainly on the two-body dissociation channels (spectra for the $D^+ + D + D$ channel can be found in Ref. [27]). Figure 6 shows KER distributions for a series of intensities at 7-fs, together with KER–$\cos\theta$ distributions at 10^{16} W/cm^2, for the $D^+ + D_2$ (left column) and $D + {D_2}^+$ (right column) channels. Also shown for comparison are data at 10^{16} W/cm^2 for 40-fs. We note that θ defines the angle between the molecular dissociation axis and the laser polarization. Each of the spectra potentially has losses at very low KER (below ~ 0.2 eV) due to blocking by the Faraday cup in our setup (see Fig. 2), which has recently been overcome with an improved setup [28].

Following the analysis in Ref. [28], the main dissociation pathways contributing to the $D^+ + D_2$ spectra at 7-fs are those marked by the arrows *A* and *B* in the Floquet dressed-states pathway diagram in Fig. 7(c). For the unacquainted, in Floquet terminology the molecular electronic states are dressed by the number of absorbed photons, denoted by $-n\omega$ (e.g., Refs. [28,44]). For example, $|2^1A' - 3\omega\rangle$ refers to the $2^1A'$ state with three photons absorbed. The expected KER is the difference in energy between that of the initial bound vibrational state and the dissociation limit at $R = \infty$. However, some deviation from these predicted values can be expected from strong-field distortion of the multiphoton curve-crossings and from internal vibrational excitation of the resulting D_2 fragment. Specifically, the main pathways marked by the arrows are *A*, $|X^1A' - 0\omega\rangle \rightarrow |2^1A' - 3\omega\rangle \rightarrow |X^1A' -$

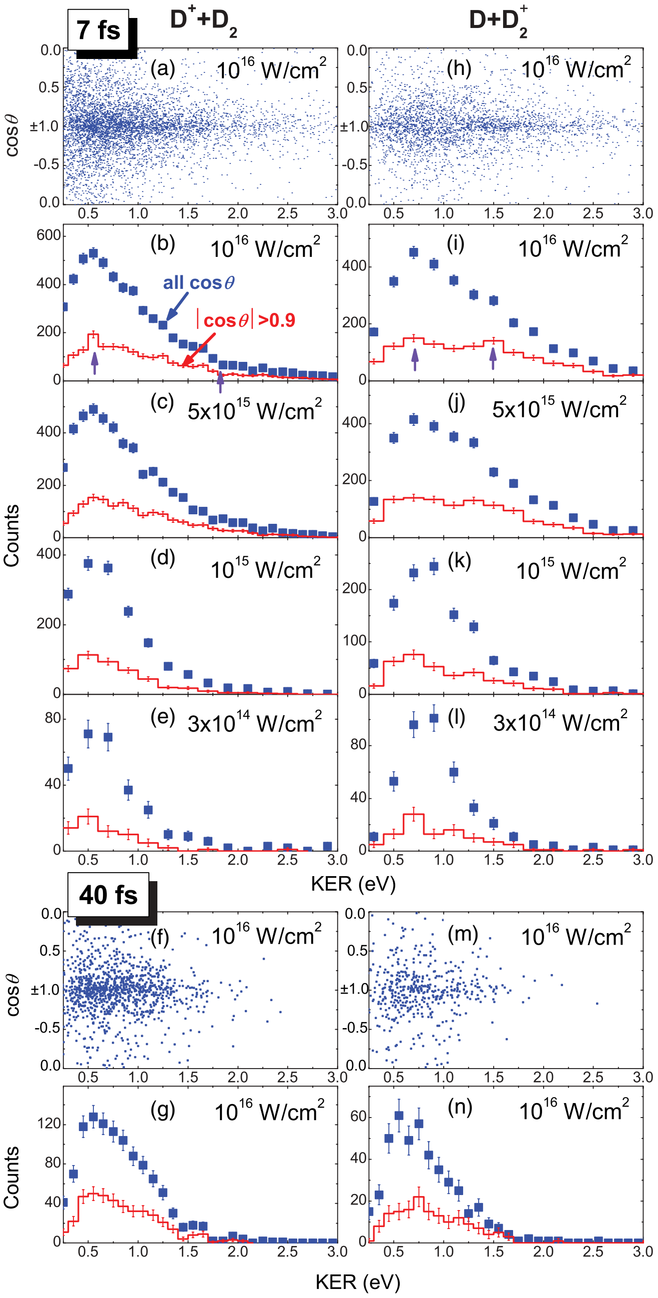

FIG. 6. (Color online) KER and angular ($\cos\theta$) distributions for two-body dissociation of ${D_3}^+$ in intense 790-nm laser pulses. The left column [panels (a)–(g)] are for the $D^+ + D_2$ channel and the right column [panels (h)–(n)] are for the $D + {D_2}^+$ channel. The upper panels [(a)–(e) and (h)–(l)] are for 7-fs and the lower panels [(f), (g), (m), and (n)] are for 40-fs. For the KER distributions, the data points show the events integrated over all $\cos\theta$ while the lines are for a slice where $|\cos\theta| > 0.9$. Peak intensities are as labeled. In the scatter plots, each data point represents a single fragmentation event while the point size varies between plots for best visualization.

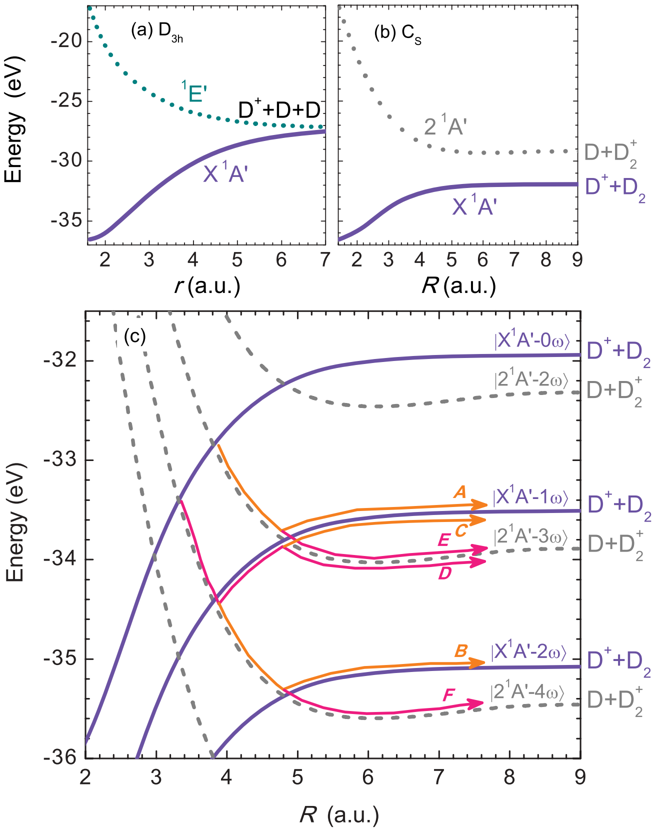

FIG. 7. (Color online) Potential energy curves for the ground and first-excited states of $D_3{}^+$ along the reaction coordinate for (a) three-body breakup [D_{3h} symmetry] and (b) two-body breakup [C_S symmetry]. Potential curves have been calculated by Talbi and Saxon [45]. (c) Floquet dressed-states potential energy diagram of $D_3{}^+$ in C_S symmetry showing pathways A, B, and C that lead to fragmentation to $D^+ + D_2$ and pathways D, E, and F that lead to fragmentation to $D + D_2{}^+$.

$1\omega\rangle$, which yields a KER of $\sim$0.55 eV, and B, $|X^1A' - 0\omega\rangle \rightarrow |2^1A' - 4\omega\rangle \rightarrow |X^1A' - 2\omega\rangle$, leading to KER $\sim$ 1.8 eV. There is also an additional dominant pathway marked by arrow C, $|X^1A' - 0\omega\rangle \rightarrow |2^1A' - 4\omega\rangle \rightarrow |X^1A' - 1\omega\rangle$ that yields a low KER of about 0.2 eV, but it is not measured in these data due to the loss of low KER breakup [28].

The peaks of the two pathways contributing to the $D^+ + D_2$ spectra, expected around 0.55 eV (pathway A) and 1.8 eV (pathway B), are marked by the small arrows in Fig. 6(b). Analysis of subsequent panels reveals that, with decreasing intensity, the higher KER peak ($\sim$1.8 eV) diminishes, resulting in the apparent shift of the weight of the distribution towards lower KER. Although these peaks are not well defined in the data, the intensity dependence is consistent with the pathway for the 1.8-eV peak (pathway B) requiring the initial absorption of four photons for the transition $X^1A' \rightarrow 2^1A'$ compared with only three photons for the peak at $\sim$0.55 eV (pathway A); see Ref. [46] for guidance on transition rules. The angular distribution in the KER–$\cos\theta$ plot shows that dissociation preferentially occurs when the two-body breakup axis is aligned along the laser polarization. The overall distribution adheres to $\sim\cos^4\theta$ as shown by the fit in Fig. 8(a), while the peak at 0.55 eV has a slightly broader angular component.

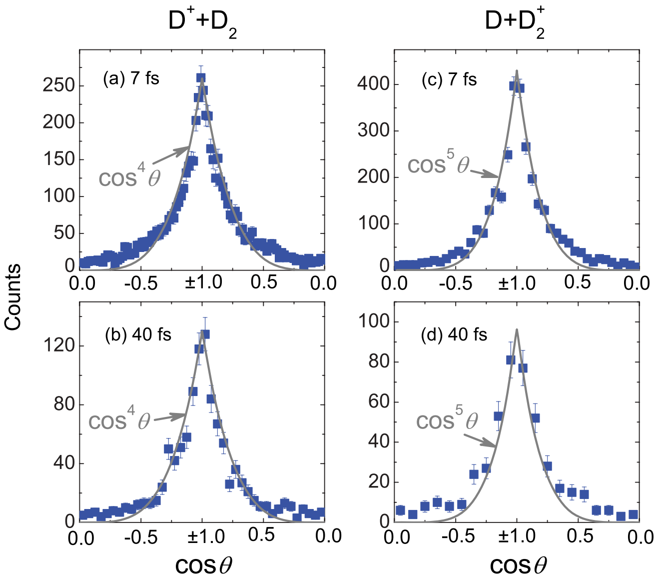

FIG. 8. (Color online) Angular ($\cos\theta$) distributions for two-body dissociation of $D_3{}^+$ corresponding to the data in Fig. 6 at 10^{16} W/cm^2. The symbols are for the experimental data, with error bars representing the statistical uncertainty, while the solid lines are fits to the data as indicated.

Comparing this data to the 40-fs $D^+ + D_2$ spectra, we do not find any substantial differences with the exception that the high-KER tail is more suppressed at 40-fs, suggesting the dominance of the lower photon-number pathway A for 40-fs.

2. $D + D_2{}^+$ *channel*

It was previously established in Ref. [28] that the $D + D_2{}^+$ spectra also have two main pathways, D and E, shown in Fig. 7(c). Pathway D, $|X^1A' - 0\omega\rangle \rightarrow |2^1A' - 4\omega\rangle \rightarrow |X^1A' - 1\omega\rangle \rightarrow |2^1A' - 3\omega\rangle$, leads to KER of about 0.6 eV, while pathway E, $|X^1A' - 0\omega\rangle \rightarrow |2^1A' - 3\omega\rangle$, gives KER $\sim$ 1.0 eV. A slice of the data for $|\cos\theta| > 0.9$ does indeed show two peaks; however, the higher KER peak is at somewhat higher energy ($\sim$1.5 eV) than the Floquet analysis suggests for pathway E ($\sim$1.0 eV). We conjecture that this may in fact be due to the involvement of a third pathway, $|X^1A' - 0\omega\rangle \rightarrow |2^1A' - 4\omega\rangle$, marked as F in Fig. 7, which has a higher KER of about 2.1 eV. This would give the illusion of the peak being skewed to higher KER and is consistent with the intensity dependence that shows that the higher KER component decreases faster at lower intensities. The new pathway F at 2.1 eV is a *net* four-photon process while the pathways at 0.6 and 1.0 eV are both *net* three-photon processes. The overall angular distribution for this channel is marginally more sharply peaked than the $D^+ + D_2$ channel displaying $\cos^5\theta$ along the laser polarization as shown in Fig. 8(c). The main difference for 40-fs is the suppression of the higher KER peak. It is not entirely clear why this is the case but one may speculate that, in longer pulses, pathways involving fewer photons dominate on the rising edge of the laser pulse.

Finally, we note that both the $D^+ + D_2$ and $D + D_2{}^+$ channels have a very weak KER component around 7 eV at 10^{16} W/cm^2 (not shown) that is about two orders of magnitude smaller than the main features shown in Fig. 6. This very high KER is the theme of a separate discussion [27] and is assigned to frustrated tunneling ionization [47] leading to electron recombination into Rydberg orbitals of the D_2 and D fragments for the respective channels, as first reported for molecules in H_2 [48].

3. $D^+ + D + D$ *channel*

As is visible in Fig. 3, the rate of three-body dissociation into $D^+ + D + D$ is extremely low. This is consistent with the PESs of $D_3{}^+$ in Figs. 4(a) and 4(b) that show that it is energetically preferable for $D_3{}^+$ to dissociate via either of the two-body channels rather than the three-body $D^+ + D + D$ channel. Indeed, the potential curves for three-body breakup in Fig. 7(a) [D_{3h} symmetry] compared with those for two-body breakup in Fig. 7(b) [C_S symmetry] show that the $D^+ + D + D$ separated-atoms limit is about 4.4 eV above the $D^+ + D_2$ limit and about 1.6 eV above the $D + D_2{}^+$ limit. The higher slope of the three-body breakup channel (see Fig. 3) is also consistent with the larger number of photons involved. Due to the low dissociation rate to $D^+ + D + D$ we will not analyze this channel in detail like the other dissociation channels. Nevertheless, we note that at 7-fs, 10^{16} W/cm^2, the dissociation mechanism for this channel is dominated by frustrated tunneling ionization [47,48] as outlined in our work elsewhere [27].

C. Single ionization

1. $D^+ + D_2{}^+$ *channel*

Single ionization of $D_3{}^+$, via the transient $D_3{}^{2+}$ PES (cuts shown in Fig. 9), leads to two-body and three-body breakup into $D^+ + D_2{}^+$ and $D^+ + D^+ + D$, respectively. The KER and angular distributions for these fragmentation channels in 7- and 40-fs pulses are displayed in Fig. 10. In the case of three-body breakup we define θ' as the angle between the normal vector to the molecular fragmentation plane, $\vec{n}$, and the laser polarization, $\vec{\varepsilon}$ (see Fig. 1).

The $D^+ + D_2{}^+$ spectra at 7-fs depend on intensity as one would expect. That is, at 10^{16} W/cm^2 the KER spectrum peaks at KER $= 7.5$ eV, which is consistent with ionization at a D–D internuclear distance of $R \sim 3.3$ a.u., determined from a cut of the PES along this dissociation direction as shown in Fig. 9(b). With decreasing intensity the spectra shift to lower KER of 5.8 eV at $\sim 10^{15}$ W/cm^2, indicating ionization at $R \sim 4.3$ a.u. This shift reflects the fact that the energy gap between the

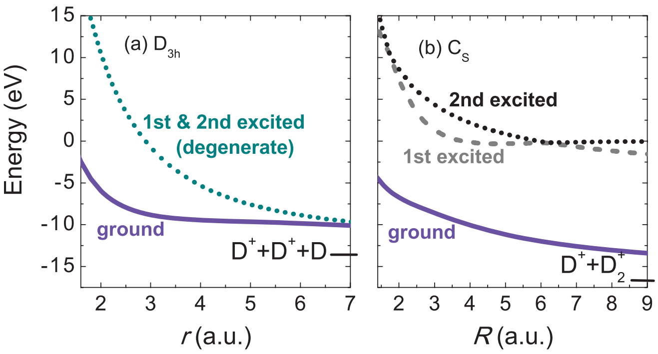

FIG. 9. (Color online) Cuts of the potential energy surfaces shown in Fig. 5 for the ground, first-excited, and second-excited states of $D_3{}^{2+}$ along the reaction coordinate for (a) three-body breakup [D_{3h} symmetry] and (b) two-body breakup [C_S symmetry]. Note that, in (a), the first- and second-excited states are degenerate, while in (b), they separate in energy, leading to a conical intersection. In (b), we use fixed $r = 2.0$ corresponding to the equilibrium distance of $D_2{}^+$.

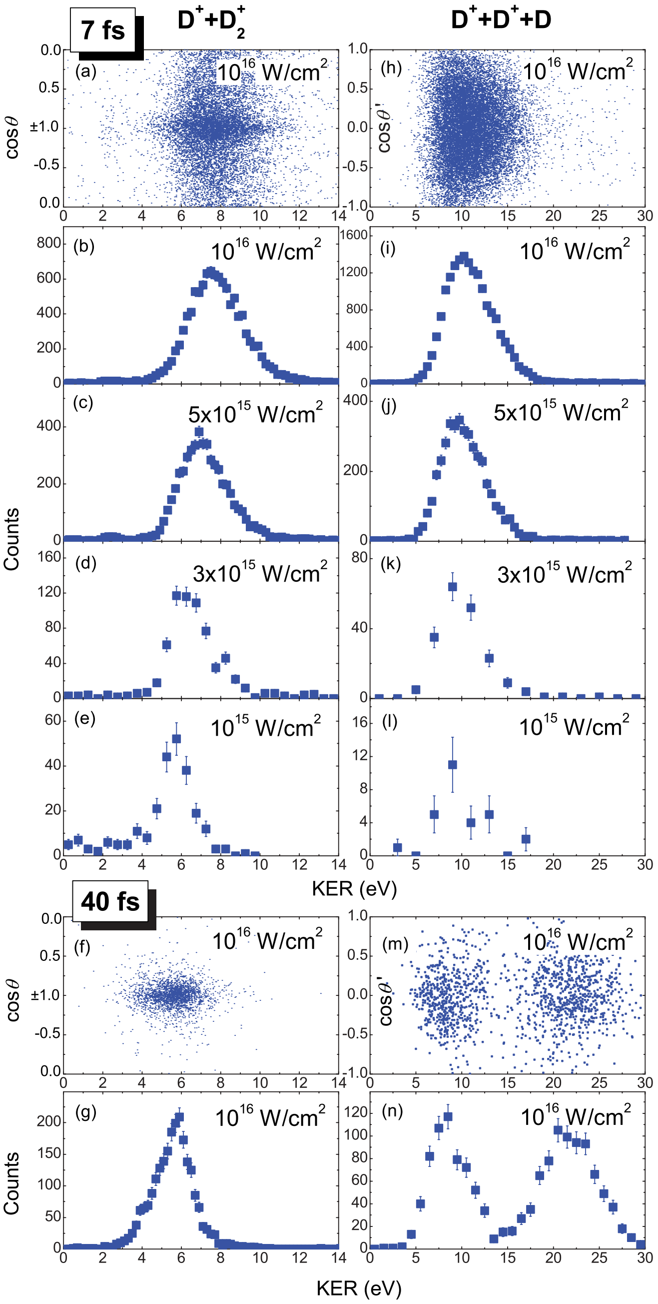

FIG. 10. (Color online) KER and angular (cos θ and cos θ') distributions for single ionization of $D_3{}^+$ in intense 790-nm laser pulses. The left column [panels (a)–(g)] are for the $D^+ + D_2{}^+$ two-body channel and the right column [panels (h)–(n)] are for the $D^+ + D^+ + D$ three-body channel. The upper panels [(a)–(e) and (h)–(l)] are for 7-fs and the lower panels [(f)–(g) and (m)–(n)] are for 40-fs. Note that for two-body breakup, θ defines the angle between the molecular dissociation axis and the laser polarization, while for three-body breakup, θ' is the angle between the normal vector to the molecular fragmentation plane and the laser polarization. Intensities are as labeled. In the scatter plots, each data point represents a single fragmentation event while the point size varies between plots for best visualization.

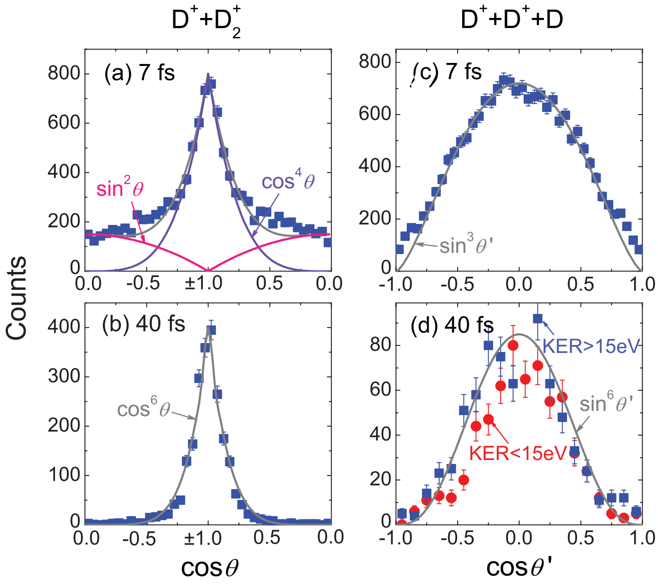

FIG. 11. (Color online) Angular ($\cos\theta$ and $\cos\theta'$) distributions for single ionization of D_3^+ corresponding to the data in Fig. 10 at 10^{16} W/cm^2. The symbols are for the experimental data, with error bars representing the statistical uncertainty, while the solid lines are fits to the data as indicated. In panel (d), slices of the experimental data are presented for the KER range indicated.

D_3^+ and D_3^{2+} PESs decreases at larger R and thus for lower intensity ionization may only occur where the energy gap is smaller. We note, however, that these R values are considerably larger than that found in the classical simulations of Lötstedt *et al.* [15], who found that ionization occurs at an average value of $R = 1.9 \pm 0.2$ a.u. and thus led to the KER distribution being peaked around 11 eV, a factor of $\sim$1.5 higher. Lötstedt *et al.* ascribed the discrepancy to inaccuracies in their model D_3^+ ground state PES. The KER will also be sensitive to the initial vibrational state distribution of D_3^+. While Lötstedt *et al.* [15] state that they use a similar vibrational energy distribution to that assumed in the experiment, it still remains a possible source of differences between experiment and theory.

The angular distribution for the $D^+ + D_2^+$ channel at 7-fs, 10^{16} W/cm^2 is quite intriguing, as seen in Fig. 11(a). It displays what appears to be two components, a dominant aligned component conforming to $\sim\cos^4\theta$ and an additional broad component that may be fitted with $\sim\sin^2\theta$. That this is the case is evident at 40-fs where the $\sin^2\theta$ component is suppressed in Fig. 11(b) and only the aligned feature remains (albeit slightly narrower, $\cos^6\theta$). This would indicate that the ionization process involves more than one pathway and, moreover, involves excitation of the D_3^+ molecule first. The pathway responsible for the $\sin^2\theta$ component is seemingly accessible at 7-fs, and not at 40-fs, showing that there is a sensitivity to the time scale for fragmentation.

2. $D^+ + D^+ + D$ *channel*

For the $D^+ + D^+ + D$ channel at 7-fs we observe a similar shift of the KER to lower values with decreasing intensity—from 10 eV at 10^{16} W/cm^2 to 9.2 eV at 3×10^{15} W/cm^2, which indicates ionization at $r \sim 3.5$ a.u. and $r \sim 3.7$ a.u., respectively [determined from the potential curves in Fig. 9(a)]. We find that the KER distribution for this channel is broader than for the $D^+ + D_2^+$ channel, as reproduced by the simulations of Lötstedt *et al.* [15,16]. Lötstedt *et al.* indicate that this is a result of the final bound electron energy distribution of D_2^+ (in the $D^+ + D_2^+$ channel) being narrower than that of D (in the $D^+ + D^+ + D$ channel); otherwise the D_2^+ would dissociate [15,16]. Thus the total kinetic energy spread for the $D^+ + D^+ + D$ channel is higher than for the $D^+ + D_2^+$ channel, leading to an overall broader energy distribution [15,16].

The most striking difference at 40-fs compared to 7-fs in our experiments is the additional large peak centered at 22 eV in Fig. 10(n). There are hints of this feature in the 7-fs data also but it is much weaker relative to the main low KER peak (and therefore is not visible in the figures). This feature is equivalent to that produced in the classical simulations [15,16], where it was assigned to frustrated tunneling ionization and the recombination of an ejected electron into the Rydberg orbital of the deuteron (see Refs. [47,48] for the original reports of this effect). Since the screening of the highly excited electron in the Rydberg D atom is negligible, the KER is very similar to that of the double-ionization channel $D^+ + D^+ + D^+$ as visible in Fig. 13(e). We present a more complete discussion of this feature with further experimental evidence in Ref. [27].

The angular distributions ($\cos\theta'$) in Figs. 10(h) and 10(m) (see note [49] on plot definitions) of the $D^+ + D^+ + D$ channel at both 7 and 40-fs show that single ionization preferentially occurs when the laser polarization is in the plane of the molecule, matching $\sim\sin^3\theta'$ for 7-fs and $\sim\sin^6\theta'$ for 40-fs as shown by the fits in Figs. 11(c) and 11(d), respectively. One can qualitatively understand this from the images of the electron cloud distribution in Fig. 1. Clearly, when the laser polarization is within the molecular plane the extent of the electron wave function is larger than when it is out of the molecular plane, which according to molecular-orbital Ammosov-Delone-Krainov (MO-ADK) theory [50] leads to a higher tunnel ionization rate.

For three-body fragmentation, another angle of importance is χ, the angle between the projection of the laser polarization in the molecular plane and the direction of a chosen fragment, for example, D. We refer the interested reader to Ref. [12], where the relevant plots for 7 and 40-fs are displayed and discussed. In summary, there is a strong preference for single ionization when the laser polarization projection is along the D fragmentation direction, for both 7- and 40-fs pulses. Again using MO-ADK theory, the χ preference is explained by the fact that the electron cloud of the dissociating D_3^{2+} is extended toward the D fragment, giving a higher tunnel ionization rate for the laser polarization in that direction. However, we do note that at 40-fs there is additionally a weaker preference for ionization when the laser polarization is perpendicular to the D direction, an observation that is in need of further explanation from theory.

Finally, before proceeding we review the energy sharing of the fragments in the three-body channel as this provides insight into the nuclear dynamics. A convenient method of displaying this information is using a Dalitz (or ternary) plot [51]. Specific details of Dalitz plots may be found elsewhere (e.g., Refs. [52–55]). Effectively, they display the relative energy of each fragment after breakup. To aid interpretation we display a momentum vector configuration diagram in Fig. 12(a).

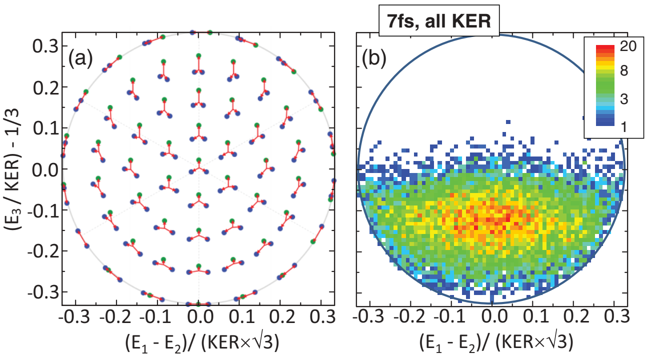

FIG. 12. (Color online) Dalitz plot of the final energy sharing of the fragments of D_3^+ single ionization leading to $D^+ + D^+ + D$ three-body breakup. Panel (a) illustrates the positions of different final momentum vector configurations (see text) while panel (b) is the experimental data for 7-fs, 10^{16}-W/cm^2, 790-nm pulses for the whole range of KER. Note that the energies of the two D^+ nuclei have been randomly assigned as E_1 and E_2 and are indistinguishable, while the energy of the D nuclei is assigned E_3.

Events that map to the center of the circle indicate that the three fragments share the final energy equally, with opposing momentum vectors, and are denoted by an equilateral triangle. Events that map to the edge of the circle indicate the breakup of the fragments with momenta vectors in a linear configuration and are denoted by linear shapes. For linear momentum configurations, there may be the following possibilities: (a) one slow (or stationary) fragment along with two fast fragments moving in opposite directions to one another. Such events will be distributed at the top right, top left, and bottom edges of the circle along the azimuthal angles $\phi = 30^\circ$, 150°, and 270°, respectively. (b) One fast fragment moving in the opposite direction to two slower fragments. These events would be distributed at the top, bottom left, and bottom right edges of the circle along $\phi = 90^\circ$, 210°, and 330°, respectively. All other positions within the diagram are some mixture of these final momentum vector configurations with the relative energy sharing denoted by the sketches. The energy of the D fragment is denoted by E_3 while the energies of the two D^+ nuclei are randomly denoted E_1 and E_2.

The spread of the experimental data for 7-fs in Fig. 12(b) shows that, in general, the D atom is less energetic than the D^+ nuclei, as the majority of events map to the lower half of the plot. This demonstrates that as the nuclei move apart during fragmentation the internuclear distance between the D^+–D^+ nuclei increasingly becomes larger than the distance between the D^+–D nuclei. This observation is consistent with the classical simulations of Lötstedt *et al.* [15], where these distances are plotted as a function of time (see Fig. 4(c) in Ref. [15]). Classically, this behavior can be understood as the D^+ ions Coulomb repelling one another, forcing each other apart, with no effect on the neutral D atom.

D. Double ionization

1. $D^+ + D^+ + D^+$ *channel*

Double ionization into $D^+ + D^+ + D^+$ leads to Coulomb explosion of the nuclei on the purely repulsive D_3^{3+} PES.

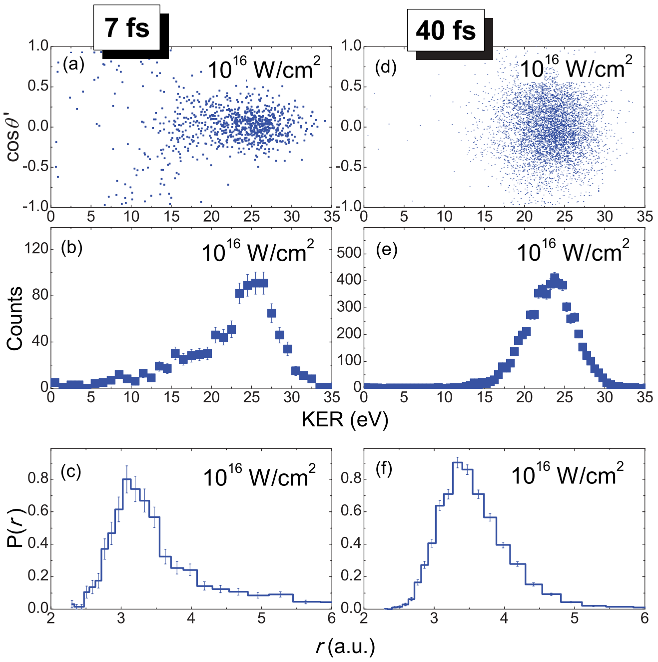

FIG. 13. (Color online) KER and angular ($\cos\theta'$) distributions, as well as retrieved internuclear r distribution immediately prior to excitation to D_3^{3+} PES (see text), for double ionization of D_3^+ leading to $D^+ + D^+ + D^+$ in intense 790-nm laser pulses. The left column [panels (a)–(c)] are for 7-fs and the right column [panels (d)–(f)] are for 40-fs, all at 10^{16} W/cm^2. In the scatter plots, each data point represents a single fragmentation event while the point size varies between plots for best visualization.

The KER and corresponding angular distributions for 7 and 40-fs are displayed in Fig. 13 at 10^{16} W/cm^2. If one assumes that the nuclei breakup as an equilateral triangular configuration (which we show momentarily to be a fairly good approximation), with internuclear distance r, then the potential energy along the r coordinate is given by $3/r$ (in atomic units) and the r distribution at the instant of ionization to the D_3^{3+} surface may be retrieved. This is shown in Figs. 13(c) and 13(f). For 7-fs, the distribution is peaked at $r = 3.2$ a.u., and only slightly higher for 40-fs at $r = 3.4$ a.u. In our ion source, D_3^+ is produced vibrationally excited with an initial r distribution centered around $r \sim 3.0$ a.u. (see Ref. [30] for an estimate of the vibrational population). Thus our retrieved distribution of r indicates that there is minimal stretching of the nuclei in transit from the initial D_3^+ ground state en route to the final D_3^{3+} state. This outcome is rather remarkable considering many other small molecules tend to stretch substantially on the intermediate states before final ionization, particularly for longer pulse durations [3,36,56]. We believe the lack of stretching can be attributed to the fact that D_3^+ is difficult to dissociate or ionize in the first place—for example, under similar conditions (7-fs, 5×10^{15} W/cm^2) we find that the rate of dissociation of D_3^+ (into $D^+ + D_2$) is a factor of ~80 lower than for H_2^+ [34]. Therefore, double ionization tends to be a direct (vertical) process.

One aspect that stands out when comparing the KER distributions at 7 and 40-fs is the low energy tail below ~12 eV at 7-fs that is absent at 40-fs. This weak tail in Fig. 13(a) displays a different angular distribution for $\cos\theta'$ (roughly

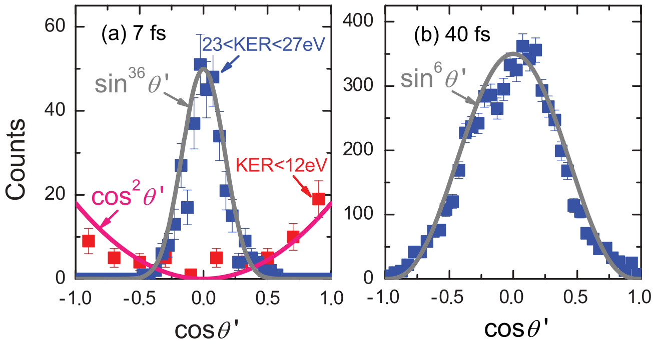

FIG. 14. (Color online) Angular ($\cos\theta'$) distributions for double ionization of $D_3{}^+$ corresponding to the data in Fig. 13 at 10^{16} W/cm^2. The symbols are for the experimental data, with error bars representing the statistical uncertainty, while the solid lines are fits to the data as indicated. In panel (a), slices of the experimental data are presented for the KER range indicated.

conforming to $\cos^2\theta'$) than the main peak ($\sim\sin^{36}\theta'$), as shown in Fig. 14(a), with many of the events occurring when the laser polarization is out of the molecular plane. Note that the main peak is also considerably broader, $\sim\sin^{6}\theta'$, at 40-fs as visible in Fig. 14(b). We pursue further the origin of the low KER events at 7-fs by examining a Dalitz plot of the energy sharing of the fragments shown in Fig. 15.

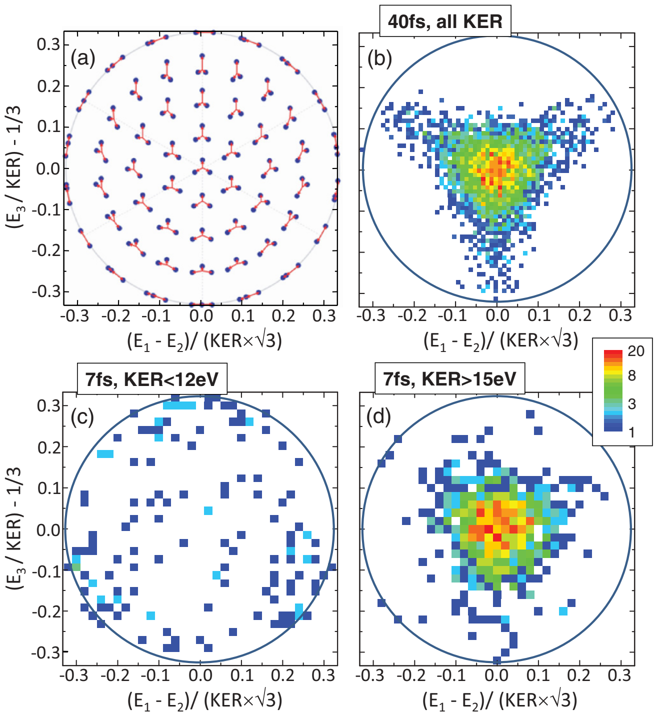

FIG. 15. (Color online) Dalitz plots of the final energy sharing of the fragments of $D_3{}^+$ double ionization leading to three-body breakup into $D^+ + D^+ + D^+$. Panel (a) illustrates the positions of different final momentum vector configurations (see text). Panel (b) is the experimental data for 40-fs, 10^{16}- W/cm^2, 790-nm pulses for the whole range of KER, while panels (c) and (d) are the same for 7-fs but for KER $<$ 12 eV and KER $>$ 15 eV only, respectively. Note that since the fragments are indistinguishable, E_1, E_2, and E_3 randomly denote the energies of the three D^+ nuclei.

Reviewing first the 40-fs data in Fig. 15(b), the majority of the distribution is concentrated around the center of the plot, showing that predominantly the fragments share the energy roughly equally, with opposing momentum vectors, consistent with Coulomb explosion from a nearly equilateral triangular configuration. There are weaker spokes of the distribution, however, that extend along $\phi = 30°$, 150°, and 270° towards the edge of the plot, showing that some molecules do break up with the final fragment momentum vectors in a linear configuration. In this linear momentum vector configuration, one D^+ fragment is nearly stationary while the other D^+ fragments move apart in opposite directions with equal and higher energy. Although in principle, a stable linear state of $D_3{}^+$ does exist ($^3\Sigma_u^+$), it is unlikely that it is populated in our ion source as it is only weakly bound and it has never been observed in experiments involving ion-beam spectroscopy [57]. Thus, the breakup of $D_3{}^+$ in a line represents a significant deviation from the initial equilateral triangle structural configuration. We note that while some deviation away from an equilateral triangle geometry will be caused by the asymmetric breathing, and bending, vibrational modes of $D_3{}^+$, the distortion may also result from structural deformation caused by the strong-field interaction [58,59].

The 7-fs plots in Figs. 15(c) and 15(d) provide insight into the origin of the low KER tail. There are two different contributions to the fragmentation spectra, one leading to KER below 12 eV and the other to KER above 15 eV. The majority of the events that correlate with KER $>$ 15 eV map to the center of the Dalitz plot as shown in Fig. 15(d). As discussed for 40-fs, this coincides with breakup with nearly equal energy sharing of the D^+ nuclei. Interestingly, the "spokes" that are present along $\phi = 30°$, 150°, and 270° for 40-fs [Fig. 15(b)] are considerably less pronounced for 7-fs in conjunction with less deformation occurring on the rising edge of the laser pulse for 7-fs (for a similar effect, see O_3 experiments [58]).

The events with KER $<$ 12 eV in Fig. 15(c) show instead a tendency to cluster around the top, bottom left, and bottom right of the plot along $\phi = 90°$, 210°, and 330°, respectively. If a trend can be inferred from the limited number of events measured here, then these positions indicate final momentum vectors where one D^+ fragment has high energy and the other two have lower (near equal) energies. In the past it has been observed for the triatomic molecules CS_2 [10] and O_3 [58] that fragmentation can result from a two-step breakup mechanism. For $D_3{}^+$ this would involve $D_3{}^{3+} \rightarrow D^+ + D_2{}^{2+} \rightarrow D^+ + D^+ + D^+$ and would be consistent with the production of one higher-energy D^+ nuclei as, in a naïve picture, the D^+ fragment would carry away two-thirds of the energy released in the first step. However, we note that for O_3 the signature of these events in a Dalitz plot was "hornlike" structures along $\phi = 30°$, 150°, and 270° (see Fig. 6(d) of Ref. [58]) rather than along $\phi = 90°$, 210°, and 330° as observed here. Matsuda *et al.* [58] also observed for O_3 that the two-step mechanism was more pronounced for 40-fs pulses than 9-fs pulses, yet we do not observe these events in our 40-fs measurements.

In Ref. [58], for O_3 some events are observed along $\phi = 90°$, 210°, and 330° and, although not explicitly stated, we understand from the discussion of Matsuda *et al.* that they are due to random (false) coincidence events. That is, fragments from two or more different molecules are wrongly correlated. In the work presented here, every effort has been made to distinguish true coincidence events from false coincidences. By limiting the laser-molecule interaction probability to much less than one per laser shot and enforcing momentum conservation, false coincidences should be negligible. Moreover, we cannot reproduce the features in Fig. 15(c) by simulating random coincidences from measured events. It will be interesting to see if future theory shows any indication of two-step breakup as it does not seem to appear in the classical simulations of Lötstedt *et al.* [15,16].

IV. SUMMARY

In summary, we have crossed a beam of $D_3{}^+$ ions with intense 7- and 40-fs, 790-nm laser pulses, with peak intensities up to 10^{16} W/cm^2, and measured the resulting fragmentation dynamics using two- and three-body coincidence 3D momentum imaging.

For the main dissociation channels, $D^+ + D_2$ and $D + D_2{}^+$, we find that higher order dissociation pathways, which open with increasing intensity at 7-fs, are absent for 40-fs. The three-body dissociation channel, $D^+ + D + D$, only becomes apparent at the highest measured intensities ($>10^{15}$ W/cm^2).

For single ionization, the $D^+ + D_2{}^+$ channel at 7-fs displays an unusual component of breakup, not present at 40-fs, in which the molecular axis prefers to be perpendicular to the strong laser field, as well as a more prominent aligned component. The $D^+ + D^+ + D$ channel displays a striking high KER feature that can be assigned to electron recombination via the frustrated tunneling ionization mechanism [27].

For double ionization leading to $D^+ + D^+ + D^+$, plots of the energy sharing of the fragments present some surprising features. Specifically, at 40-fs a small component of molecular breakup is found to deviate from an equilateral triangular configuration for momentum vectors of the final fragments, to a nearly linear configuration of the momentum vectors, a signature of structural deformation. At 7-fs, we report tentative evidence for the possibility of a two-step breakup mechanism. In all cases of ionization, we find only minimal stretching of the $D_3{}^+$ molecule prior to ionization, even for 40-fs pulses.

We hope that the results presented here may instigate and provide a benchmark for theoretical studies of this fundamental system. As demonstrated recently by Lötstedt *et al.* [15,16], important steps in this direction have already been made. While full quantum-mechanical treatment is likely to be some time away, a classical treatment can still capture many of the salient features of the dynamics of $D_3{}^+$.

ACKNOWLEDGMENTS

We are indebted to Z. Chang's group for providing expertise with the laser beams and C. W. Fehrenbach for his help with the ion beams. We also are grateful to C. B. Madsen for sharing calculations of the $D_3{}^+$ orbital images shown in Fig. 1 and to B. D. Esry for stimulating discussions on this work. J.M.K. acknowledges interesting discussions with E. Lötstedt. This work was supported by the Chemical Sciences, Geosciences, and Biosciences Division, Office of Basic Energy Sciences, Office of Science, US Department of Energy.

---

[1] C. D. Lin, A.-T. Le, Z. Chen, T. Morishita, and R. Lucchese, J. Phys. B **43**, 122001 (2010).

[2] R. Dörner, T. Weber, M. Weckenbrock, A. Staudte, M. Hattass, H. Schmidt-Böcking, R. Moshammer, and J. Ullrich, Adv. At. Mol. Opt. Phys. **48**, 1 (2002).

[3] J. H. Posthumus, Rep. Prog. Phys. **67**, 623 (2004).

[4] J. Ullrich, R. Moshammer, A. Dorn, R. Dörner, L. P. H. Schmidt, and H. Schmidt-Böcking, Rep. Prog. Phys. **66**, 1463 (2003).

[5] I. Ben-Itzhak, P. Q. Wang, J. F. Xia, A. M. Sayler, M. A. Smith, K. D. Carnes, and B. D. Esry, Phys. Rev. Lett. **95**, 073002 (2005).

[6] M. Odenweller, N. Takemoto, A. Vredenborg, K. Cole, K. Pahl, J. Titze, L. P. H. Schmidt, T. Jahnke, R. Dörner, and A. Becker, Phys. Rev. Lett. **107**, 143004 (2011).

[7] J. S. Parker, B. J. S. Doherty, K. T. Taylor, K. D. Schultz, C. I. Blaga, and L. F. DiMauro, Phys. Rev. Lett. **96**, 133001 (2006).

[8] F. Anis and B. D. Esry, Phys. Rev. A **77**, 033416 (2008).

[9] T. Niederhausen, U. Thumm, and F. Martin, J. Phys. B **45**, 105602 (2012).

[10] A. Hishikawa, H. Hasegawa, and K. Yamanouchi, Chem. Phys. Lett. **361**, 245 (2002).

[11] H. Xu, T. Okino, and K. Yamanouchi, J. Chem. Phys. **131**, 151102 (2009).

[12] J. McKenna, A. M. Sayler, B. Gaire, N. G. Johnson, K. D. Carnes, B. D. Esry, and I. Ben-Itzhak, Phys. Rev. Lett. **103**, 103004 (2009).

[13] J. D. Alexander, C. R. Calvert, R. B. King, O. Kelly, L. Graham, W. A. Bryan, G. R. A. J. Nemeth, W. R. Newell, C. A. Froud, I. C. E. Turcu *et al.*, J. Phys. B **42**, 141004 (2009).

[14] C. B. Madsen (private communication).

[15] E. Lötstedt, T. Kato, and K. Yamanouchi, Phys. Rev. Lett. **106**, 203001 (2011).

[16] E. Lötstedt, T. Kato, and K. Yamanouchi, Phys. Rev. A **85**, 053410 (2012).

[17] D. S. Tchitchekova, H. Lu, S. Chelkowski, and A. D. Bandrauk, J. Phys. B **44**, 065601 (2011).

[18] H. Yu, T. Zuo, and A. D. Bandrauk, J. Phys. B **31**, 1533 (1998).

[19] A. D. Bandrauk and J. Ruel, Phys. Rev. A **59**, 2153 (1999).

[20] A. D. Bandrauk, S. Chelkowski, and I. Kawata, Phys. Rev. A **67**, 013407 (2003).

[21] M. Lein, P. P. Corso, J. P. Marangos, and P. L. Knight, Phys. Rev. A **67**, 023819 (2003).

[22] X. B. Bian, L. Y. Peng, and T. Y. Shi, Phys. Rev. A **78**, 053408 (2008).

[23] H. Yu and A. D. Bandrauk, Phys. Rev. A **56**, 685 (1997).

[24] A. D. Bandrauk and H. Yu, Phys. Rev. A **59**, 539 (1999).

[25] I. Kawata, H. Kono, and A. D. Bandrauk, Phys. Rev. A **64**, 043411 (2001).

[26] H. Yu and A. D. Bandrauk, J. Chem. Phys. **102**, 1257 (1995).

[27] J. McKenna, A. M. Sayler, B. Gaire, N. G. Johnson, B. D. Esry, K. D. Carnes, and I. Ben-Itzhak [New J. Phys. (to be published)].

[28] B. Gaire, J. McKenna, M. Zohrabi, K. D. Carnes, B. D. Esry, and I. Ben-Itzhak, Phys. Rev. A **85**, 023419 (2012).

[29] P. Q. Wang, A. M. Sayler, K. D. Carnes, J. F. Xia, M. A. Smith, B. D. Esry, and I. Ben-Itzhak, Phys. Rev. A **74**, 043411 (2006).

[30] V. G. Anicich and J. H. Futrell, Int. J. Mass Spectrom. Ion Phys. **55**, 189 (1984).

[31] H. Mashiko, C. M. Nakamura, C. Li, E. Moon, H. Wang, J. Tackett, and Z. Chang, Appl. Phys. Lett. **90**, 161114 (2007).

[32] I. D. Williams, J. McKenna, J. Wood, M. Suresh, W. A. Bryan, S. L. Stebbings, E. M. L. English, C. R. Calvert, B. Srigengan, E. J. Divall *et al.*, Phys. Rev. Lett. **99**, 173002 (2007).

[33] J. McKenna, M. Suresh, D. S. Murphy, W. A. Bryan, L.-Y. Peng, S. L. Stebbings, E. M. L. English, J. Wood, B. Srigengan, I. C. E. Turcu *et al.*, J. Phys. B **40**, 2607 (2007).

[34] A. M. Sayler, P. Q. Wang, K. D. Carnes, and I. Ben-Itzhak, J. Phys. B **40**, 4367 (2007).

[35] P. Hansch, M. A. Walker, and L. D. Van Woerkom, Phys. Rev. A **54**, R2559 (1996).

[36] J. McKenna, M. Suresh, B. Srigengan, I. D. Williams, W. A. Bryan, E. M. L. English, S. L. Stebbings, W. R. Newell, I. C. E. Turcu, J. M. Smith *et al.*, Phys. Rev. A **73**, 043401 (2006).

[37] B. Gaire, A. M. Sayler, P. Q. Wang, N. G. Johnson, M. Leonard, E. Parke, K. D. Carnes, and I. Ben-Itzhak, Rev. Sci. Instrum. **78**, 024503 (2007).

[38] A. Ichihara and K. Yokoyama, J. Chem. Phys. **103**, 2109 (1995).

[39] A. Rudenko, B. Feuerstein, K. Zrost, V. L. B. de Jesus, T. Ergler, C. Dimopoulou, C. D. Schröter, R. Moshammer, and J. Ullrich, J. Phys. B **38**, 487 (2005).

[40] A. S. Alnaser, X. M. Tong, T. Osipov, S. Voss, C. M. Maharjan, P. Ranitovic, B. Ulrich, B. Shan, Z. Chang, C. D. Lin *et al.*, Phys. Rev. Lett. **93**, 183202 (2004).

[41] F. Légaré, I. V. Litvinyuk, P. W. Dooley, F. Quéré, A. D. Bandrauk, D. M. Villeneuve, and P. B. Corkum, Phys. Rev. Lett. **91**, 093002 (2003).

[42] W. A. Bryan, S. L. Stebbings, E. M. L. English, T. R. J. Goodworth, W. R. Newell, J. McKenna, M. Suresh, B. Srigengan, I. D. Williams, I. C. E. Turcu *et al.*, Phys. Rev. A **73**, 013407 (2006).

[43] A. M. Sayler, Ph.D. thesis, Kansas State University, 2008.

[44] J. McKenna, A. M. Sayler, F. Anis, B. Gaire, N. G. Johnson, E. Parke, J. J. Hua, H. Mashiko, C. M. Nakamura, E. Moon *et al.*, Phys. Rev. Lett. **100**, 133001 (2008).

[45] D. Talbi and R. P. Saxon, J. Chem. Phys. **89**, 2235 (1988).

[46] A. M. Sayler, P. Q. Wang, K. D. Carnes, B. D. Esry, and I. Ben-Itzhak, Phys. Rev. A **75**, 063420 (2007).

[47] T. Nubbemeyer, K. Gorling, A. Saenz, U. Eichmann, and W. Sandner, Phys. Rev. Lett. **101**, 233001 (2008).

[48] B. Manschwetus, T. Nubbemeyer, K. Gorling, G. Steinmeyer, U. Eichmann, H. Rottke, and W. Sandner, Phys. Rev. Lett. **102**, 113002 (2009).

[49] Note that in the three-body case, for the KER–$\cos\theta'$ distribution, $\cos\theta'$ is plotted from -1 to $+1$, unlike $\cos\theta$ in the two-body case, which is plotted from 0 to -1 and then from $+1$ to 0. The axis of the two-body fragmentation, and the molecular plane of three-body fragmentation, is aligned along the center of the plots and an isotropic distribution would produce a uniform distribution in $\cos\theta$ or $\cos\theta'$, respectively.

[50] X. M. Tong, Z. X. Zhao, and C. D. Lin, Phys. Rev. A **66**, 033402 (2002).

[51] R. H. Dalitz, Philos. Mag. **44**, 1068 (1953).

[52] D. Strasser, L. Lammich, S. Krohn, M. Lange, H. Kreckel, J. Levin, D. Schwalm, Z. Vager, R. Wester, A. Wolf *et al.*, Phys. Rev. Lett. **86**, 779 (2001).

[53] U. Muller, T. Eckert, M. Braun, and H. Helm, Phys. Rev. Lett. **83**, 2718 (1999).

[54] D. Babikov, E. A. Gislason, M. Sizun, F. Aguillon, V. Sidis, M. Barat, J. C. Brenot, J. A. Fayeton, and Y. J. Picard, J. Chem. Phys. **116**, 4871 (2002).

[55] C. M. Laperle, J. E. Mann, T. G. Clements, and R. E. Continetti, Phys. Rev. Lett. **93**, 153202 (2004).

[56] B. Gaire, J. McKenna, N. G. Johnson, A. M. Sayler, E. Parke, K. D. Carnes, and I. Ben-Itzhak, Phys. Rev. A **79**, 063414 (2009).

[57] J. Tennyson, Rep. Prog. Phys. **57**, 421 (1995).

[58] A. Matsuda, E. J. Takahashi, and A. Hishikawa, J. Chem. Phys. **127**, 114318 (2007).

[59] A. M. Sayler *et al.* (unpublished).